Giant enhancement of exciton diffusion near an electronic Mott insulator

Pranshoo Upadhyay[1,2,*], Daniel G. Suárez-Forero[1,*,†], Tsung-Sheng Huang[1,*], Mahmoud Jalali Mehrabad[1], Beini Gao[1], Supratik Sarkar[1,2], Deric Session[1], Kenji Watanabe[3], Takashi Taniguchi[3], You Zhou[4,5], Michael Knap[6,7], Mohammad Hafezi[1,‡]

[1]Joint Quantum Institute, University of Maryland, College Park, MD 20742, USA.

[2]Department of Electrical and Computer Engineering, University of Maryland, College Park, MD 20742, USA.

[3]Research Center for Materials Nanoarchitectonics, National Institute for Materials Science, 1-1 Namiki, Tsukuba 305-0044, Japan.

[4]Department of Materials Science and Engineering, University of Maryland, College Park, MD 20742, USA.

[5]Maryland Quantum Materials Center, College Park, Maryland 20742, USA.

[6]Technical University of Munich, TUM School of Natural Sciences, Physics Department, 85748 Garching, Germany.

[7]Munich Center for Quantum Science and Technology (MCQST), Schellingstr. 4, 80799 München, Germany.

Corresponding authors. Email: † dsuarezf@umd.edu, ‡ hafezi@umd.edu

*These authors contributed equally to this work.

Bose-Fermi mixtures naturally appear in various physical systems. In semiconductor heterostructures, such mixtures can be realized, with bosons as excitons and fermions as dopant charges. However, the complexity of these hybrid systems challenges the comprehension of the mechanisms that determine physical properties such as mobility. In this study, we investigate interlayer exciton diffusion

in an H-stacked WSe_2/WS_2 heterobilayer. Our measurements are performed in the dilute exciton density limit at low temperatures to examine how the presence of charges affects exciton mobility. Remarkably, for charge doping near the Mott insulator phase, we observe a giant enhancement of exciton diffusion of three orders of magnitude compared to charge neutrality. We attribute this observation to mobile valence holes, which experience a suppressed moiré potential due to the electronic charge order in the conduction band, and recombine with any conduction electron in a non-monogamous manner. This new mechanism emerges for sufficiently large fillings in the vicinity of correlated generalized Wigner crystal and Mott insulating states. Our results demonstrate the potential to characterize correlated electron states through exciton diffusion and provide insights into the rich interplay of bosons and fermions in semiconductor heterostructures.

Layered transition metal dichalcogenides (TMDs) have become an interesting platform to study collective emerging electronic phenomena, including Mott insulators (*1–3*), generalized Wigner crystals (*4, 5*), density waves (*6*), fractional Chern insulators (*7, 8*), quasi-exciton condensation (*9*), superconductivity (*10, 11*), and kinetic ferromagnetism (*12*). One remarkable direction is to use optical excitons to probe various electronic orders (*13*). Since excitons can be generally considered as bosons, hybrid electron-exciton systems provide a natural platform for investigating Bose-Fermi mixtures. Bose-Fermi mixtures are ubiquitous in many-body physics, from solutions of fermionic ^{3}He in bosonic superfluid ^{4}He (*14*), and quark-meson models in QCD physics (*15, 16*), to ultracold atoms (*17–20*).

Recent experimental implementations of Bose-Fermi mixtures in TMDs (*21–26*) have motivated the search for exotic physics such as tunable particle interactions (*27, 28*), and topological superconductivity (*29, 30*). A key challenge is to understand how excitons behave in correlated electronic environments. Measuring the transport of excitons immersed in an electron gas has the potential to address this challenge. Although this technique has been proven effective in exploring the rich physics of TMD systems (*31–39*), the high exciton occupation considered in these demonstrations prevents probing fermionic correlations. Here, we explore the limit in which a very dilute concentration of bosons (excitons) diffuses in a 2D fermionic (electronic) gas to investigate how the rich phases of the fermionic many-body system affect the dynamics of bosons.

Our system consists of a WSe_2/WS_2 moiré heterostructure where we employ space- and time-resolved techniques to study diffusing interlayer excitons (IXs) immersed in a 2D fermionic electron gas. Our measurements reveal that the exciton diffusion coefficient is highly sensitive to changes in the electronic filling of the system. We analyze exciton dynamics within the various exotic electronic states that are realized by our system, uncovering a rich landscape dominated by polarons, generalized Wigner crystals, and a Mott-insulating state. Depending on the electronic state, we observe dramatic variations in the mobility of the diffusing species, with changes up to three orders of magnitude. Our results challenge the common assumption that electrons and holes forming IXs always move together in a monogamous manner, particularly near the Mott-insulating state. With the help of an effective model Hamiltonian, an interplay of two different channels for the diffusion of excitonic species is demonstrated. These findings present a novel optical approach for exploring complex quantum states in condensed matter systems.

1 Physical system

The experimental setup and moiré system are depicted in Fig. 1a. The system consists of an H-stacked WS_2/WSe_2 bilayer heterostructure hosting a triangular moiré lattice (see Supplementary Material). Optically exciting this system creates IX that form between spatially separated electrons and holes residing in different moiré registries (*40*). The nature and dynamics of IX is determined by the state of the electron gas (Fig. 1a). The spatially resolved photoluminescence (PL) emission, which is broader than the diffraction-limited optical excitation, encodes the information of IX diffusion (Fig. 1b-c). The excitation pump is resonant with the WSe_2 intralayer exciton in all our measurements (upper panel of Fig. 1d). Upon ultra-fast electron transfer (in the order of femtoseconds (*41*)), the IX form, diffuse, and optically recombine (lower panel of Fig. 1d). As mentioned earlier, in this work we focus on the ultra-low exciton density regime where exciton-exciton interactions are negligible. Hence, the system can be treated as individual bosons moving within a gas of fermions.

To identify this regime, we look at the collected PL spectrum of IX as a function of the electron filling (ν_e) for different pump intensities. Details on the calibration of ν_e are provided in Supplementary Note 1. Figure 1e-f displays the normalized PL spectra for two pump intensities (80

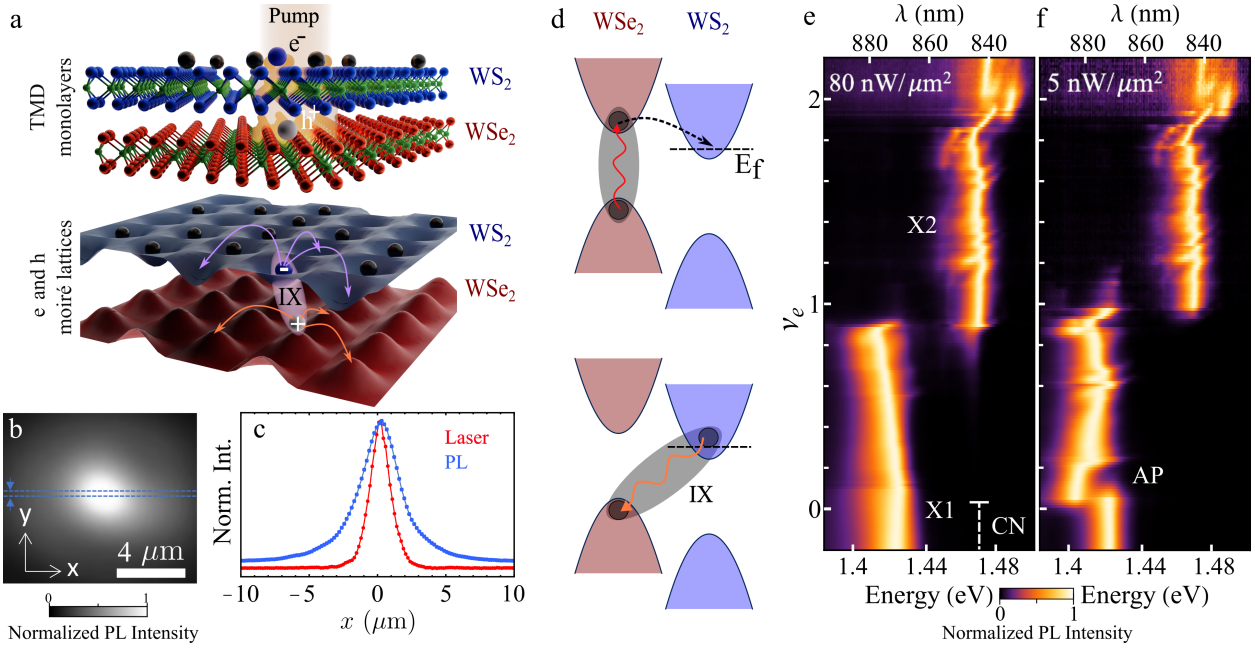

Figure 1: **Description of the experimental scheme and characterization of the physical system.** (a) Schematic of the diffusion setup for the extraction of IX hopping strength in the moiré system in a doped environment. (b) Image of the IX PL when excited with a diffraction-limited laser spot. (c) The spatial variation of PL intensity (blue) along the x-axis within the region indicated by the blue dashed line in (b) is compared to that of the laser spot (red). The difference between the laser profile and the PL profile originates in the diffusion of the excitonic population. (d) IX creation in the bilayer sample. A resonant laser creates a population of excitons in the WSe_2 layer (upper panel). Due to the band alignment, the electron tunnels from the WSe_2 to the WS_2 and forms an IX that diffuses and recombines radiatively. Normalized PL spectrum of IX at 3.5 K as a function of electronic filling factor, ν_e at (e) moderate (80 nW/μm^2) and (f) ultra-low (5 nW/μm^2) excitation pump intensity. The blue-shift at $\nu_e \sim 1$ indicates the Mott gap ($U_{ex-e} \sim 46$ meV). The polaron gap (~ 16 meV) is observed only at ultra-low pump intensities.

nW/μm^2 and 5 nW/μm^2). For both exciton densities, the charge neutral (CN) region is dominated by a low-energy IX (X1) which transitions into a high-energy exciton (X2) at $\nu_e \sim 1$. The transition is benchmarked by a $\sim$46 meV gap in the PL emission, and it has been recently demonstrated to arise from the strong on-site exciton-electron repulsions owing to the formation of an electronic Mott-insulating state at $\nu_e \approx 1$ (*21–23*). Although the system's response in the Mott insulating state is similar for both pump intensities, there is a clear difference at low electron densities: in the ultra-low exciton density case (panel f) an additional gap of $\sim$ 16 meV is observed near $\nu_e = 0$. This redshift corresponds to the transition from X1 to attractive polaron (AP), as corroborated by the diffusion measurements discussed later. The AP formation is facilitated in such an H-stacked system where the hole can bind with multiple nearest neighboring electrons (*40*); more details regarding the AP formation can be found in Supplementary Note 2. Understanding the precise nature of the AP in the presence of a lattice is an open problem and will be an interesting future research direction both experimentally and theoretically. Here, we identify the AP with the dressed charge complex comprised of X1 and dopant charges. It is important to note that AP formation occurs in both cases when the system is doped, however, a complete transition into AP can only be observed when the ratio of X1 to electron density is small; in other words, when each exciton can be dressed by surrounding electrons. This observation is validated by even lower pump intensity ($<$ 5 nW/μm^2) measurements, as shown in Supplementary Note 3. All the presented data has been taken in this low-pump intensity regime unless stated otherwise.

In this low-pump intensity regime, we identify four distinct spectral features as a function of electron doping as shown in Fig. 1f. The extracted intensity and energy values are shown in Fig. 2a-b, and they can be distinguished as follows:

1. Charge-neutral region: dominated by X1 emission,
2. Moderate-doping region ($1/7 < \nu_e < 6/7$): largely dominated by AP, except at certain fractional fillings (e.g. 1/3, 2/3, and 6/7) that host correlated states.
3. Mott-insulating region ($6/7 < \nu_e < 1$): dominated by X1. The strong electron localization inhibits the formation of APs in this region.
4. High-doping region ($\nu_e > 1$): dominated by X2 due to double occupancy of moiré sites (doublon-hole pair).

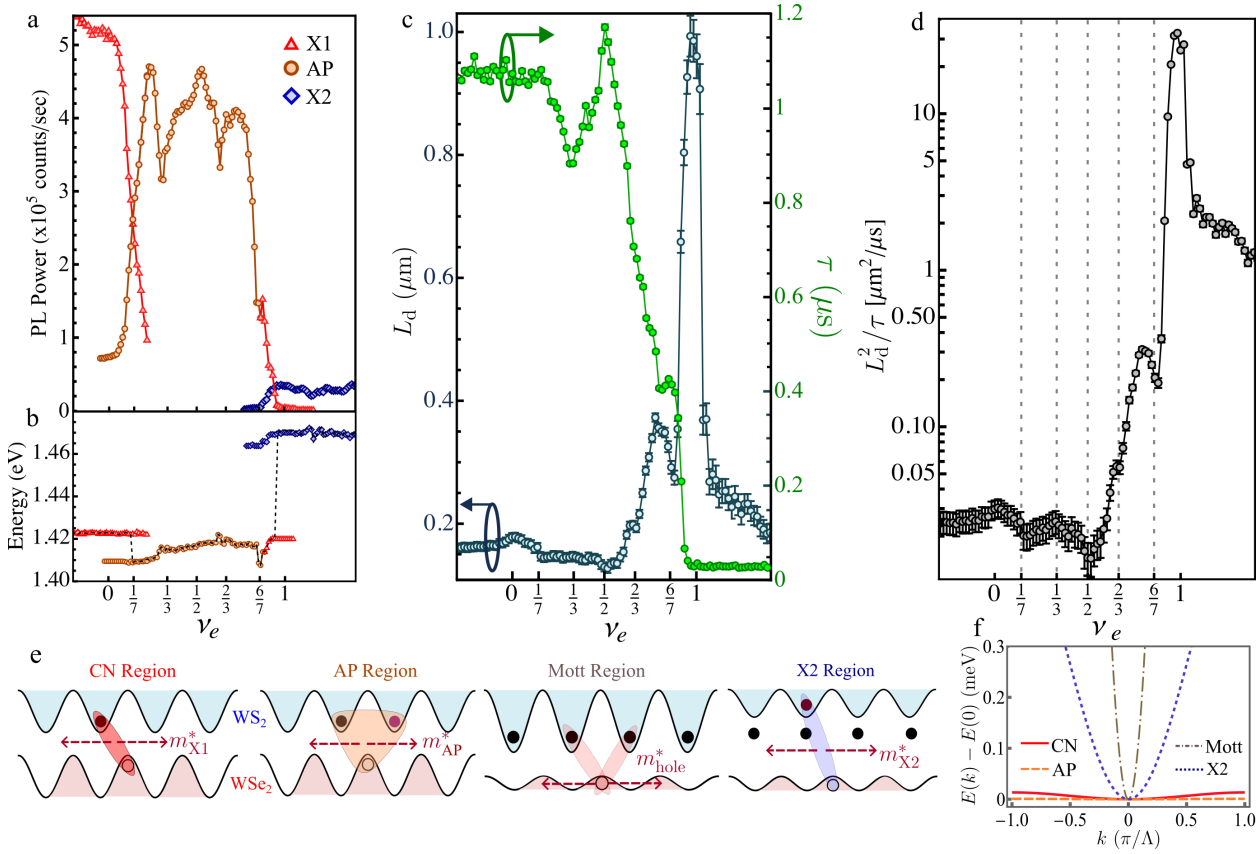

Figure 2: **Space- and time-resolved measurements of interlayer quasiparticle dynamics in an electron-doped lattice.** (a) Integrated PL of X1, AP, and X2 as a function of doping aids in identifying different regimes of fermionic filling, including the onset of the AP and the Mott-insulating region. (b) Peak energy tracking as a function of doping. (c) Diffusion length (L_d shown in blue) and IX lifetime (τ shown in green) as a function of electron doping. Both quantities strongly vary around fractional and integer fillings. (d) Diffusivity, $D = \frac{L_\mathrm{d}^2}{\tau}$, demonstrates the variation of the tunneling rate of interlayer quasiparticles. Remarkably, more than three orders of magnitude enhancement in D is observed near the Mott-insulating state. All measurements are collected at a temperature of 3.5 K. (e) Four fermionic regions highlighting variation of tunneling species are demonstrated. The shifted moiré lattice for holes and electrons represents the H-stacked system. AP being heavier than X1 results in lower D. For the case of $\nu_\mathrm{e} \sim 1$, X1 does not tunnel as a composite particle rather the hole moves in a non-monogamous way. In this configuration, the effective potential for holes in the Mott region is reduced. For even larger fillings $\nu_\mathrm{e} \gtrsim 1$, X2 tunnels in an effectively reduced moiré potential. (f) Energy dispersion of the diffusing particles, shown in (e), calculated for these regions (color encoded) indicate the variation of the effective mass (m^*) in the system.

Having identified the four different doping regimes, we now measure the diffusion dynamics of the quasiparticles of each regime and their dependence on the density of the 2D electron gas.

2 Exciton diffusion mechanisms

We extract the diffusion length from the spatially-resolved PL emission by employing a Gaussian fitting routine and analyze it as a function of ν_e. Considering that the measured PL profile corresponds to a convolution between quasiparticle diffusion and laser intensity distribution, the diffusion length is given by $L_\mathrm{d} = \sqrt{\sigma_\mathrm{X}^2 - \sigma_\mathrm{L}^2}$, where σ_X and σ_L correspond to the half-widths of the PL and laser profiles, respectively. More details about the fitting procedure are given in SM. The obtained values for the diffusion length are displayed as blue markers in Fig. 2c. In the CN region, the diffusion length is less than 200 nm; over an order of magnitude lower than previously reported measurements in structures without a moiré lattice (*42, 43*). Such a suppression in diffusion length indicates that the IX kinetic energy is quenched by the presence of a strong moiré potential in our system. Further suppression of L_d is observed upon doping the system, i.e. in the region dominated by AP. Remarkably, a significant enhancement of L_d is noticed as the system is further doped to $\nu_\mathrm{e} \sim 1$, followed by a significant drop in the regime dominated by X2. For further clarity, spectrally resolved diffusion is shown in Supplementary Note 4.

A complete analysis of the IX mobility requires the measurement of its lifetime (τ), as the modulations in diffusion can originate either from the tunneling rate variation or the quasiparticle's lifetime. We measure this quantity by using a femtosecond pulsed laser with a repetition rate of $\sim$500 kHz while the signal is collected in a superconducting single photon detector (see Methods). The observed lifetime as a function of ν_e is shown with green markers in Fig. 2c. We notice a trend of lifetime reduction with doping, and modulations at some fractional fillings. In agreement with previous reports (*24*), τ decreases by over an order of magnitude, from ~ 1 μs in the CN region to $\sim$30 ns in the Mott region. The reduction in τ and enhancement of L_d in the Mott region suggests the presence of highly mobile particles with low effective mass.

Assuming that the dynamics is diffusive, we can use the diffusion coefficient ($D = L_\mathrm{d}^2/\tau$) to study different regimes. We observe a remarkable three-orders of magnitude enhancement of the mobility at the Mott-insulating region, see Fig. 2d. This intriguing behavior can be counter-intuitive

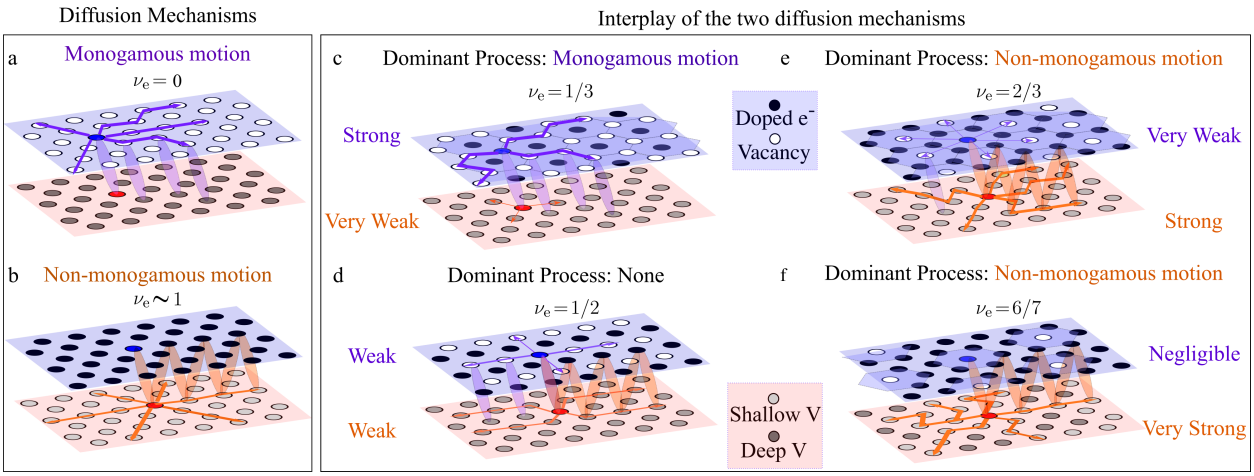

Figure 3: **Illustration of the exciton diffusion mechanisms.** The two diffusion channels that determine the motion of optically created electron (blue circle) and hole (red circle) pairs are displayed in panels (a) and (b). Black and white circles in the electron layer indicate electronically filled and vacant sites, respectively. Light-gray and dark-gray circles in the hole layer indicate shallow and deep effective hole potentials. (a) At $\nu_e = 0$, only monogamous IX motion is possible. (b) For $\nu_e \sim 1$, the only channel is the non-monogamous hole hopping. The interplay of these two channels is represented for the following filling fractions: (c) $\nu_e = 1/3$, (d) $\nu_e = 1/2$, (e) $\nu_e = 2/3$, and (f) $\nu_e = 6/7$. Available NN vacant sites enhance monogamous motion, while NN electron-doped sites enhance non-monogamous hole hopping. The trend reverses at $\nu_e = 1/2$, where both processes are effectively suppressed.

at first, as high mobility contrasts with the insulating nature of the electron gas. To comprehend this anomalous behavior, we analyze how the changes in ν_e lead to the renormalization of the diffusing particle's effective mass (m^*). This effect originates from the Coulomb potential (V_{Coul}) exerted by the electron gas on the diffusing particles. The addition of V_{Coul} and the moiré potential, together with changes in the mass of the diffusing particles determine the large variations in m^*. An effective model to describe this behavior (*44*) and the extracted values of m^* for each doping region are presented in Supplementary Note 5.

The four physical situations depicted in Fig. 2e describe how the electrons affect D. With the mentioned model, we estimate the energy dispersion of the diffusing particles for each case (Fig. 2f). For the CN region, as $V_{\text{Coul}} \approx 0$, the electron and hole experience a similar potential

landscape in their respective layers, favoring their motion together as a bound particle. As expected for moiré-trapped excitons, we observe a diffusion coefficient several orders of magnitude lower than the values reported for IX in the absence of moiré potential (*43*). In the AP region, where V_{Coul} remains comparatively negligible, we detect an increase in the effective mass m^*_{AP}. The formation of heavier quasiparticles resulting from the dopant electrons dressing the injected optical excitons leads to the observed reduction in mobility. The decreasing trend in D reverses at $\nu_{\mathrm{e}} = 1/2$. This phenomenon is discussed in more detail in the next section.

The dramatic three-orders-of-magnitude increase in mobility near the Mott region can be attributed to the stronger effective potential in the electron layer and the suppressed potential in the hole layer, as depicted in Fig. 2e. This significant variation in effective potential results from the crystallization of electrons, which generates V_{Coul} with the same period and phase as the electron moiré lattice but out of phase with the hole moiré lattice as holes occupy different atomic registry. Additionally, due to the absence of any vacancies in the electron layer, the hole in the other layer is free to hop into any moiré site. Hence, in the Mott region, the hole is not bound to a specific electron and can recombine with any electron in the lattice in a non-monogamous way. This non-monogamous hopping, combined with the reduced effective potential depth, leads to a decrease in m^*, accounting for the orders-of-magnitude enhancement in D. However, beyond $\nu_{\mathrm{e}} = 1$, the excited electrons become mobile again, allowing the electron and hole to move together, in contrast to the previous non-monogamous hole dynamics. This is pictorially shown in the last panel of Fig. 2e, where an additional electron on top of the electron lattice and a hole in the other layer form a diffusing exciton. Interestingly, in this X2 region, both the hole and the electron encounter shallower potentials due to the out-of-phase V_{Coul} in each layer. This shallower potential results in orders-of-magnitude increased mobility of X2 compared to X1. However, the monogamous motion manifests as a reduction in mobility compared to the holes in the Mott region. This discussion elucidates the observed strong variation in D across the four different fermionic regions.

3 Diffusion at generalized Wigner crystal states

The remarkable sensitivity of the mobility to the fermionic state of the system is further manifested at certain fractional fillings that host generalized Wigner crystals due to the long-range repulsive

interactions. Before focusing on these specific filling factors, we reiterate that the general trend of D is reversed at $\nu_e = 1/2$. This observation can be understood by analyzing the occupation of the nearest neighbor (NN) sites of the injected IX below and above $\nu_e = 1/2$. Figure 3 illustrates how, in the two regimes, the NN filling determines the interplay between the two diffusion mechanisms. At $\nu_e = 0$, where all the NN sites are vacant, only monogamous motion can take place (Fig. 3a), while for $\nu_e \sim 1$, non-monogamous motion exclusively determines the exciton mobility due to the complete occupation of the moiré sites (Fig. 3b). For any other filling, the system experiences an interplay between the two diffusion mechanisms.

To elucidate, we make a direct comparison of the available diffusion channels at $\nu_e = 1/3$ and $\nu_e = 2/3$. The monogamous motion of the exciton, allowed for $\nu_e = 1/3$, is blocked by the filled NN sites in the electron layer at $\nu_e = 2/3$ (Fig. 3c and e). Hence, one would expect lower mobility at $\nu_e = 2/3$ compared to $\nu_e = 1/3$. However, the experimental results (Fig. 2d) show a local minimum but an overall increase in D at $\nu_e = 2/3$ compared to $\nu_e = 1/3$. To understand this, we note that while the occupied NN sites hinder the monogamous motion of electron and hole, they simultaneously create non-monogamous channels that facilitate the diffusion of holes, as shown by the arrows in the bottom layer of Fig. 3e. Therefore, the increasing trend in D is a consequence of the dominant non-monogamous hole diffusion. This effect gets stronger at $\nu_e = 6/7$ as the occupation of both NN and next-nearest neighbor (NNN) sites (Fig. 3f) increases the number of diffusion channels in the hole layer. It should be noted that the local minima in D at $\nu_e = 2/3$ and $6/7$ result from the inhibition of the monogamous motion of IXs because the electrons' wavefunctions are more localized.

The interplay of the two discussed diffusion mechanisms determines the non-trivial dependence of D in the explored range of ν_e. In this picture, the dominant mechanism changes at $\nu_e = 1/2$. The monogamous motion of quasiparticles (X1 or AP) determines the mobility in the region $0 < \nu_e < 1/2$, while it is the non-monogamous hole diffusion for $1/2 < \nu_e < 1$. $\nu_e = 1/2$ (Fig. 3d) acts as the turning point, exhibiting the lowest mobility as both processes are effectively suppressed.

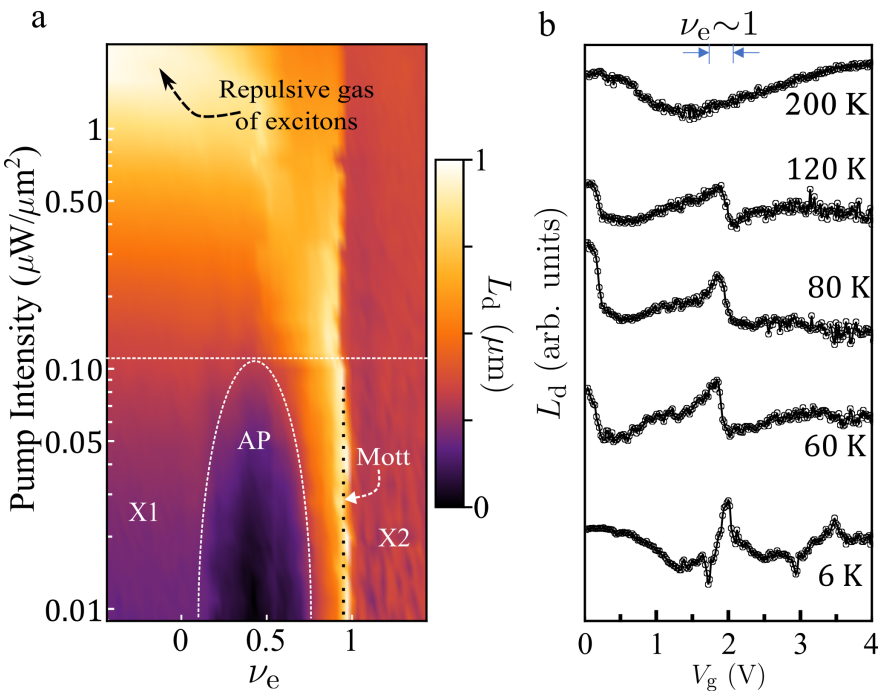

Figure 4: **Exciton density and temperature dependence of diffusion in the moiré lattice.** (a) The pump intensity-dependent variation demonstrates the threshold (horizontal white dashed line) above which IX-IX scattering mechanisms dictate the diffusion dynamics. Diffusion at pump intensities above this threshold is primarily due to annihilation and repulsion mechanisms while at ultra-low pump intensity, the diffusion originates from quasiparticle tunneling between moiré sites. The vanishing of AP and Mott features in L_d for high pump intensities demonstrates this difference. (b) Temperature dependence of L_d shows the existence of a peak around $\nu_e \sim 1$ for T < 200 K, although other features, including AP and fractional fillings, are lost. No observable feature in diffusion exists above this temperature although the Mott gap exists for the entire range of temperature used in our measurements. This is due to the enhanced phonon scattering channels that dominate the dynamics. For high temperatures, we use V_g in the horizontal axis because ν_e is not well defined.

4 Pump intensity phase map and temperature dependence

Our physical picture of the diffusion mechanisms is limited to a regime of low exciton density at cryogenic temperatures. Additional physical processes affecting the dynamics are expected to emerge for higher densities and temperatures. To gain insights into these more complex regimes, we map the dependence of the diffusion length as a function of ν_e and pump intensity. As illustrated in Figure 4a, the enhancement of the mobility near the Mott region is evident for pump intensities less than 100 nW/μm^2, indicated by the white dashed line. Beyond this pump intensity, the sharp peak associated with the Mott insulating region becomes less distinctive and shifts to lower ν_e, indicating a regime where additional processes such as double exciton occupancies and exciton-exciton scattering become relevant. The monotonic increase in L_d with pump intensity at charge neutrality (CN) suggests that these scattering processes are enhanced with the exciton density. For pump intensities greater than 1 μW/μm^2, the system enters a non-linear repulsive regime where exciton-exciton dipole repulsion dominates the diffusion dynamics. Figure 4a highlights these different regimes.

The reduction of mobility due to the formation of AP is more sensitive to exciton density. Hence, the features in this region start to fade away at around 50 nW/μm^2. In this case, the exciton to polaron transition is blurred out due to the larger population of excitons compared to the dopant electrons in the lattice.

Another crucial parameter for L_d is the temperature (T). Figure 4b shows that the diffusion peak at the Mott insulating state vanishes for $T \geq 200$ K. Although the Mott gap persists over the full measured temperature range (see Supplementary Note 6), no significant dependence of L_d with V_g is observed beyond 200 K. This is attributed to increased phonon-assisted scattering mechanisms that dominate the diffusion dynamics at higher temperatures (*45*). Additionally, the signatures of AP in the voltage regime 1 V $\lesssim V_g \lesssim$ 2 V are suppressed above 60 K, as the AP cannot form at elevated temperatures due to its low binding energy.

5 Outlook

In conclusion, we unveil the two mechanisms affecting the mobility of a dilute exciton population in an electron-doped moiré system. The demonstrated breakdown of conventional monogamous exciton diffusion and clear signatures of electronic correlations evidence the potential of this technique to probe complex states of matter.

In perspective, a broad range of physical effects can be explored by measuring the mobility of embedded particles in van der Waals structures. For example, the nature of exotic phases of matter, including kinetic magnetism (*12, 46*), exciton condensation (*47*), and anomalous quantum Hall regimes (*7, 8*), could be studied with this technique. In particular, incorporating polarization resolution and fields into this technique offers the possibility to study fractional Chern insulators (*8*), Mott-moiré excitons (*48*), spin polarons (*49*), and tunable electron-exciton interactions (*27, 28*). Moreover, the microseconds-long exciton lifetimes allow one to conceive time-resolved diffusion experiments, capable of extracting valuable insights into the temporal dynamics of fermionic correlated states.

References and Notes

1. Y. Tang, *et al.*, Simulation of Hubbard model physics in WSe2/WS2 moiré superlattices. *Nature* **579** (7799), 353–358 (2020).

2. Y. Shimazaki, *et al.*, Strongly correlated electrons and hybrid excitons in a moiré heterostructure. *Nature* **580** (7804), 472–477 (2020).

3. Y. Shimazaki, *et al.*, Optical signatures of periodic charge distribution in a Mott-like correlated insulator state. *Physical Review X* **11** (2), 021027 (2021).

4. Y. Xu, *et al.*, Correlated insulating states at fractional fillings of moiré superlattices. *Nature* **587** (7833), 214–218 (2020).

5. E. C. Regan, *et al.*, Mott and generalized Wigner crystal states in WSe2/WS2 moiré superlattices. *Nature* **579** (7799), 359–363 (2020).

6. Y. Zeng, *et al.*, Exciton density waves in Coulomb-coupled dual moiré lattices. *Nat. Mater.* **22** (2), 175–179 (2023).

7. H. Park, *et al.*, Observation of fractionally quantized anomalous Hall effect. *Nature* **622** (7981), 74–79 (2023).

8. Y. Zeng, *et al.*, Thermodynamic evidence of fractional Chern insulator in moiré MoTe2. *Nature* **622** (7981), 69–73 (2023).

9. L. Ma, *et al.*, Strongly correlated excitonic insulator in atomic double layers. *Nature* **598** (7882), 585–589 (2021).

10. Y. Xia, *et al.*, Unconventional superconductivity in twisted bilayer WSe2 (2024).

11. Y. Guo, *et al.*, Superconductivity in twisted bilayer WSe_2 (2024).

12. L. Ciorciaro, *et al.*, Kinetic magnetism in triangular moiré materials. *Nature* **623** (7987), 509–513 (2023).

13. L. Du, *et al.*, Moiré photonics and optoelectronics. *Science* **379** (6639), eadg0014 (2023).

14. C. Ebner, D. O. Edwards, The low temperature thermodynamic properties of superfluid solutions of 3He in 4He. *Phys. Rep.* **2** (2), 77–154 (1971).

15. B.-J. Schaefer, J. Wambach, The phase diagram of the quark–meson model. *Nucl. Phys. A* **757** (3-4), 479–492 (2005).

16. P. Achenbach, *et al.*, The present and future of QCD. *Nuclear Physics A* **1047**, 122874 (2024).

17. K. Günter, T. Stöferle, H. Moritz, M. Köhl, T. Esslinger, Bose-Fermi mixtures in a three-dimensional optical lattice. *Physical Review Letters* **96** (18), 180402 (2006).

18. F. Schreck, *et al.*, Sympathetic cooling of bosonic and fermionic lithium gases towards quantum degeneracy. *Physical Review A* **64** (1), 011402 (2001).

19. M.-G. Hu, *et al.*, Bose polarons in the strongly interacting regime. *Physical review letters* **117** (5), 055301 (2016).

20. M. Delehaye, I. F. Barbut, S. Laurent, A mixture of bose and fermi superfluids. *Science* **345** (6200), 1035–1038 (2014).

21. Z. Lian, *et al.*, Valley-polarized excitonic Mott insulator in WS2/WSe2 moiré superlattice. *Nat. Phys.* **20** (1), 34–39 (2023).

22. B. Gao, *et al.*, Excitonic Mott insulator in a Bose-Fermi-Hubbard system of moiré WS2/WSe2 heterobilayer. *Nat. Commun.* **15** (1), 2305 (2024).

23. R. Xiong, *et al.*, Correlated insulator of excitons in WSe2/WS2 moiré superlattices. *Science* **380** (6647), 860–864 (2023).

24. H. Park, *et al.*, Dipole ladders with large Hubbard interaction in a moiré exciton lattice. *Nat. Phys.* **19** (9), 1286–1292 (2023).

25. L. Ma, *et al.*, Strongly correlated excitonic insulator in atomic double layers. *Nature* **598** (7882), 585–589 (2021).

26. Z. Zhang, *et al.*, Correlated interlayer exciton insulator in heterostructures of monolayer WSe2 and moiré WS2/WSe2. *Nat. Phys.* **18** (10), 1214–1220 (2022).

27. C. Kuhlenkamp, M. Knap, M. Wagner, R. Schmidt, A. m. c. Imamoğlu, Tunable Feshbach Resonances and Their Spectral Signatures in Bilayer Semiconductors. *Phys. Rev. Lett.* **129**, 037401 (2022), doi:10.1103/PhysRevLett.129.037401.

28. I. Schwartz, *et al.*, Electrically tunable Feshbach resonances in twisted bilayer semicondsowinuctors. *Science* **374** (6565), 336–340 (2021).

29. C. Zerba, C. Kuhlenkamp, A. Imamoğlu, M. Knap, Realizing topological superconductivity in tunable Bose-Fermi mixtures with transition metal dichalcogenide heterostructures. *Physical Review Letters* **133** (5), 056902 (2024).

30. E. Y. Andrei, *et al.*, The marvels of moiré materials. *Nat. Rev. Mater.* **6** (3), 201–206 (2021).

31. E. Malic, R. Perea-Causin, R. Rosati, D. Erkensten, S. Brem, Exciton transport in atomically thin semiconductors. *nature communications* **14** (1), 3430 (2023).

32. J. Choi, *et al.*, Moiré potential impedes interlayer exciton diffusion in van der Waals heterostructures. *Sci. Adv.* **6** (39), eaba8866 (2020).

33. J. Wang, *et al.*, Diffusivity Reveals Three Distinct Phases of Interlayer Excitons in $MoSe_2/WSe_2$ Heterobilayers. *Phys. Rev. Lett.* **126**, 106804 (2021), doi:10.1103/PhysRevLett.126.106804.

34. C. Jin, *et al.*, Imaging of pure spin-valley diffusion current in WS2-WSe2 heterostructures. *Science* **360** (6391), 893–896 (2018).

35. Z. Sun, *et al.*, Excitonic transport driven by repulsive dipolar interaction in a van der Waals heterostructure. *Nat. Photonics* **16** (1), 79–85 (2022).

36. L. Yuan, *et al.*, Twist-angle-dependent interlayer exciton diffusion in WS2-WSe2 heterobilayers. *Nat. Mater.* **19** (6), 617–623 (2020).

37. E. Wietek, *et al.*, Nonlinear and Negative Effective Diffusivity of Interlayer Excitons in Moiré-Free Heterobilayers. *Phys. Rev. Lett.* **132**, 016202 (2024), doi:10.1103/PhysRevLett.132.016202.

38. F. Tagarelli, *et al.*, Electrical control of hybrid exciton transport in a van der Waals heterostructure. *Nat. Photonics* **17** (7), 615–621 (2023).

39. A. Rossi, *et al.*, Anomalous interlayer exciton diffusion in WS2/WSe2 moiré heterostructure. *ACS nano* (2024).

40. X. Wang, *et al.*, Intercell moiré exciton complexes in electron lattices. *Nat. Mater.* **22** (5), 599–604 (2023).

41. X. Hong, *et al.*, Ultrafast charge transfer in atomically thin MoS2/WS2 heterostructures. *Nat. Nanotechnol.* **9** (9), 682–686 (2014).

42. Z. Li, *et al.*, Interlayer Exciton Transport in MoSe2/WSe2 Heterostructures. *ACS Nano* **15** (1), 1539–1547 (2021), doi:10.1021/acsnano.0c08981.

43. J. Choi, *et al.*, Moiré potential impedes interlayer exciton diffusion in van der Waals heterostructures. *Sci. Adv.* **6** (39), eaba8866 (2020).

44. C. Lagoin, F. Dubin, Key role of the moiré potential for the quasicondensation of interlayer excitons in van der Waals heterostructures. *Physical Review B* **103** (4), L041406 (2021).

45. A. Chernikov, M. M. Glazov, Chapter Three - Exciton diffusion in 2D van der Waals semiconductors, in *2D Excitonic Materials and Devices*, P. B. Deotare, Z. Mi, Eds. (Elsevier), vol. 112 of *Semiconductors and Semimetals*, pp. 69–110 (2023), doi:https://doi.org/10.1016/bs.semsem.2023.09.001.

46. H. Yang, Y.-H. Zhang, Exciton- and light-induced ferromagnetism from doping a moiré Mott insulator. *Phys. Rev. B.* **110** (4) (2024).

47. W. Yao, Q. Niu, Berry phase effect on the exciton transport and on the exciton Bose-Einstein condensate. *Phys. Rev. Lett.* **101** (10), 106401 (2008).

48. T.-S. Huang, Y.-Z. Chou, C. L. Baldwin, F. Wu, M. Hafezi, Mott-moiré excitons. *Phys. Rev. B* **107**, 195151 (2023), doi:10.1103/PhysRevB.107.195151.

49. Z. Tao, *et al.*, Observation of spin polarons in a frustrated moiré Hubbard system. *Nature Physics* pp. 1–5 (2024).

50. L. Yuan, *et al.*, Twist-angle-dependent interlayer exciton diffusion in WS2–WSe2 heterobilayers. *Nature materials* **19** (6), 617–623 (2020).

51. B. Amin, T. P. Kaloni, U. Schwingenschlögl, Strain engineering of WS 2, WSe 2, and WTe 2. *Rsc Advances* **4** (65), 34561–34565 (2014).

Acknowledgement

The authors acknowledge fruitful discussions with Ming Xie, Ajit Srivastava, and Angel Rubio. YZ acknowledges support from the National Science Foundation under Award No. DMR-2145712. M.K. acknowledges support from the Deutsche Forschungsgemeinschaft (DFG, German Research Foundation) under Germany's Excellence Strategy–EXC–2111–390814868 and from the European Research Council (ERC) under the European Unions Horizon 2020 research and innovation programme (Grant Agreement No. 851161).

Methods

Device fabrication

The hBN encapsulated WSe_2/WS_2 heterostructures were fabricated using a dry-transfer method reported in the literature (*22*). All flakes were exfoliated from bulk crystals onto Si/SiO_2 (285 nm) and identified by their optical contrast. The top/bottom gates and TMD contact are made of few-layer graphene. The flakes were picked sequentially with a polymer stamp and released onto a Si/SiO_2 (90 nm) substrate. Later, electrodes consisting of 10 nm of chromium and 70 nm of gold were patterned on the substrate. They were fabricated using standard electron-beam lithography techniques and thermal evaporation. The sample was annealed at 300° C for 2 hr.

Optical Measurements

All the measurements are performed in a dilution refrigerator at 3.5K unless stated otherwise. The sample is excited using a Ti:Sapphire laser tuned at 733 nm, resonant to the WSe_2 intralayer exciton, and focused to diffraction limit with an 80× microscope objective. Spatially resolved images are collected in a CCD camera (Princeton Instruments Blaze HRX) coupled to a spectrograph (Princeton Instruments SP2750). The total magnification of the optical setup is ∼220×. For lifetime

measurements, we excite the sample with a 100 fs pulsed Ti:Sapphire laser. We use a pulse picker to achieve a repetition rate low enough to detect the optical decay of the long-lived IX ($\sim$500 kHz). In this case, we use a superconducting nanowire single-photon detector and an event timer module to obtain the time-correlated PL signal.

Competing interests

The authors declare no competing interests.

Data availability

All of the data that support the findings of this study are reported in the main text and Supplementary Material. Source data are available from the corresponding authors on reasonable request.

Supplementary materials

Supplementary Text

Supplementary Materials for

Giant enhancement of exciton diffusion near an electronic Mott insulator

Pranshoo Upadhyay[1,2,*], Daniel G. Suárez-Forero[1,*,†], Tsung-Sheng Huang[1,*], Mahmoud Jalali Mehrabad[1], Beini Gao[1], Supratik Sarkar[1,2], Deric Session[1], Kenji Watanabe[3], Takashi Taniguchi[3], You Zhou[4,5], Michael Knap[6,7], Mohammad Hafezi[1,‡]

[1]Joint Quantum Institute, University of Maryland, College Park, MD 20742, USA.

[2]Department of Electrical and Computer Engineering, University of Maryland, College Park, MD 20742, USA.

[3]Research Center for Materials Nanoarchitectonics, National Institute for Materials Science, 1-1 Namiki, Tsukuba 305-0044, Japan.

[4]Department of Materials Science and Engineering, University of Maryland, College Park, MD 20742, USA.

[5]Maryland Quantum Materials Center, College Park, Maryland 20742, USA.

[6]Technical University of Munich, TUM School of Natural Sciences, Physics Department, 85748 Garching, Germany.

[7]Munich Center for Quantum Science and Technology (MCQST), Schellingstr. 4, 80799 München, Germany.

Corresponding authors. Email: † dsuarezf@umd.edu, ‡ hafezi@umd.edu

*These authors contributed equally to this work.

This PDF file includes:

Supplementary Note 1. Device structure and optical characterization

We fabricate a transition metal dichalcogenide (TMD) hetero-bilayer sample for diffusion measurements. WS_2 and WSe_2 are the two monolayer TMDs used for this purpose. After aligning their edges, they are stacked to achieve 0^o twist angle, i.e., 2H stacking order. The sample is encapsulated with hBN ($\sim$ 35 nm) and gated on both sides for independent control of the out-of-plane electric field and doping. Figure S1a shows an optical micrograph of the sample. We characterize the device using reflection and photoluminescence (PL) measurements. Figures S1b and c present the reflection contrast spectrum of WSe_2 intralayer exciton and PL map of the interlayer exciton (IX) measured on the bilayer region, respectively.

Both measurements show distinctive features at the charge-neutral (CN) region ($\nu_e = 0$), the Mott-insulating region ($\nu_e = 1$), and the band-insulating region ($\nu_e = 2$). Identifying these regions is useful to calibrate the gate voltage (V_g) to ν_e. However, for better accuracy, we track the peak intensity variations of the IX species with doping as shown in Fig. 2a (Main text). Here, $\nu_e = 0$ is benchmarked by the emergence of the peak associated with the attractive polaron (AP). The presence of that peak coincides with a decrease in the X1 intensity. $\nu_e = 1$ is identified by the complete extinction of the X1 intensity. It is important to mention that a proper calibration of ν_e can only be performed at ultra-low pump intensities (a few nW/μm^2 or lower), because it relies on the features of the polaron gap, only present at these low exciton densities.

Supplementary Note 2. Formation of AP and its dependence on pump intensity

Due to the H-stacking order in this system, electrons and holes localize in different moiré registries as discussed in detail in recent literature (*40*). This lateral separation of electrons and holes is the key to the formation of interlayer AP in the system. In this configuration, a hole in the WSe_2 layer can bind with three sites in the electron layer with equal probability. This allows the hole in the bottom layer (WSe_2) to pair with a cloud of electrons in the top layer (WS_2). Due to the

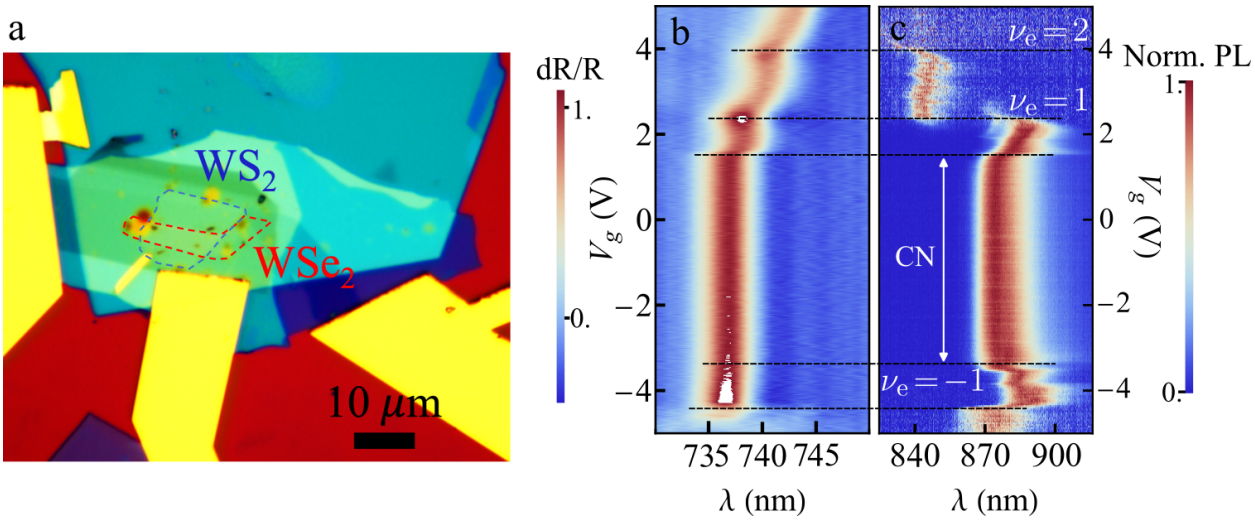

Figure S1: **WS_2/WSe_2 heterobilayer and its optical characterization.** a) The optical micrograph of the heterobilayer device. WS_2 and WSe_2 monolayer regions are indicated by the blue and red dashed lines, respectively. b) Electronic filling (ν_e)-dependent reflection contrast spectrum of WSe_2 intralayer exciton on the bilayer region indicates the Mott-insulating and band-insulating states at ν_e = 1 and 2, respectively. c) PL spectrum of IX features AP for electron and hole doping and doublon-hole pair (X2) beyond $\nu_e = \pm 1$.

complexity involved in understanding the precise nature of APs, specifically in the moiré system, we consider a trion-like charge complex, without affecting the conclusion of this work, to explain our observations. In Fig. S2a, we illustrate this exemplary case of AP where an embedded X1 binds with one doped electron. It is important to note that the additional electrons in AP, i.e. other than the optically excited one, should be from the opposite valley to avoid short-range repulsive interactions (Fig. S2b). This is not expected for R-stacked heterobilayers, because in that case, electrons and holes are confined in the same registries, leading to weak repulsive interaction between X1 and doped electrons (*40*).

It should be further noted that AP formation can be distinctively observed in PL only for ultra-low excitation power. When the density of excitons is lower than the density of doped electrons in the system, we can have each exciton associated with at least one electron, forming AP. However, here, the density of doped electrons must be small as at higher densities close to $\nu_e \sim 1$ the repulsive interactions become strong and inhibit the formation of AP. We illustrate the dependence of AP on exciton and electron density in Fig. S3. For the case of 1 nW/μm^2, we have a clear transition from

X1 to AP upon doping. This gap is observed to reduce and eventually vanish with excitation pump intensity. Additionally, AP transitions to X1 again at high electron doping close to $\nu_e \sim 1$.

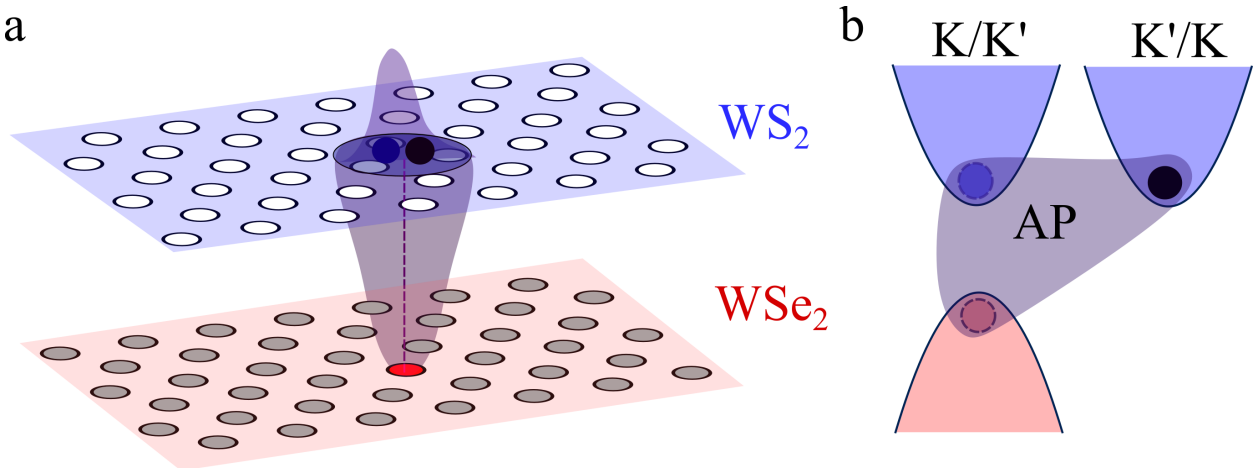

Figure S2: **Formation of interlayer AP in a moiré lattice.** a) Schematic of the AP formation in the H-stacked WS_2/WSe_2 heterostructure. Here, an exemplary case of X1 dressed by a doped electron is considered. As the hole resides in a different moiré registry than electrons, it has three electron sites with equal probability of binding. This results in the wavefunction of both the electrons spread across the three moiré sites. b) The doped electrons involved in the formation of AP must be from the opposite valley to reduce short-range repulsive interactions.

Supplementary Note 3. Ultra-low power excitation regime

Based on the above discussion regarding AP formation, we determine the dilute exciton density regime. A complete polaron gap ($\sim$ 16 meV) is used as a benchmark for achieving the dilute regime. In the main text, we have shown a complete polaron gap for 5 nW/μm^2. In Fig. S4, we demonstrate that any pump intensity below 5 nW/μm^2 will have a comparable spectrum in the entire range of doping. This confirms our regime of operation.

Supplementary Note 4. Spectrally resolved diffusion

As discussed in the main manuscript, the surge in diffusion length (L_d) near the Mott-insulating region is a novel observation that warrants a detailed analysis. In Fig. S5a, we show spectrally

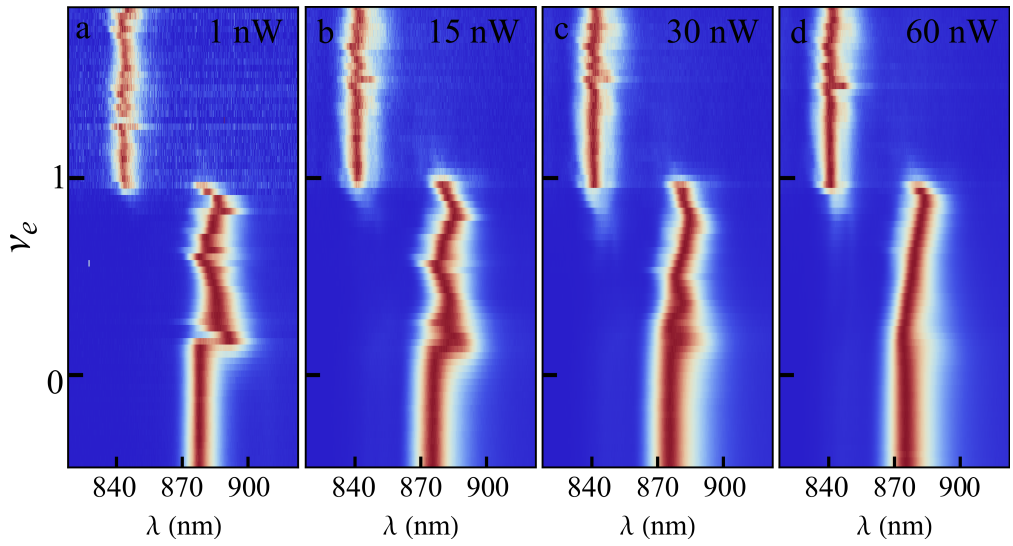

Figure S3: **Variation of polaron gap with excitation power.** The gap above the CN region gradually closes with the pump power. This confirms the presence of AP only in the dilute exciton density regime.

resolved diffusion collected by using gratings and separating the spectrum into two regions: one below 860 nm (X2) and one above (X1 or AP). We apply the Gaussian fitting routine and extract the diffusion length. As shown by the red (X1 or AP) and purple (X2) markers, diffusion near the Mott region is solely from X1. Although both X1 and X2 have similar intensity in that region (Fig. S5b), X2 demonstrates negligible diffusion. However, for $\nu_e \geq 1$, the diffusion is dominated by X2 and results in a peak near $\nu_e = 2$.

Supplementary Note 5. Doping-dependent renormalization of moiré potential

To model the variations in diffusivity with doping, we solve a simplified 1D lattice Hamiltonian: $\hat{H} = -\frac{\hbar^2}{2m}\frac{d^2}{dz^2} + \frac{V}{2}\sin\left(\frac{2\pi z}{\Lambda}\right)$. Here, m is the mass of the exciton, trion, or hole, depending on the regime of consideration, in the absence of the moiré potential. V is the total potential resulting from adding the moiré potential (V_m) and the Coulomb interactions (V_Coul) which accounts for the modification of the superlattice due the charge order, and Λ is the moiré lattice spacing. This Hamiltonian, whose eigenstates in real space are the Mathieu functions, has been successfully used

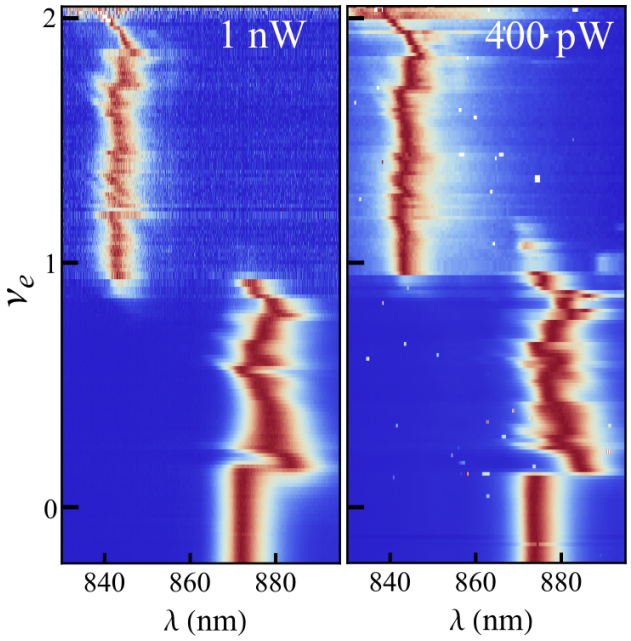

Figure S4: **PL at dilute exciton population.** PL at both 1nW/μm^2 and 400 pW/μm^2 have the same polaron gap and Mott transition conditions. This confirms the dilute exciton population regime.

to model interlayer excitons in TMD heterobilayers (*44*). Although this model does not capture the geometric details of the moiré lattice, it provides the effective mass (m^*) of diffusing particles. m^*, determined by the values of m and V in each regime, is a critical parameter due to its inverse proportionality to the mobility. Extracting the variation in m^* allows us to understand the rich behavior shown in Fig. 2d of the main text.

To evaluate the renormalization of the effective moiré potential (V) we consider certain parameters: $V_\mathrm{m} \sim 100$ meV in each layer (*50*), the mass of electron (m_e) and hole (m_h) in WS_2 and WSe_2 is considered to be 0.5 m_0 and 0.4 m_0, respectively (*51*). Here, m_0 is the free electron mass. The list of m, V and m^* values for the diffusing particle in the corresponding fermionic region are listed in Table S1. For the charge-neutral (CN) region, V for X1 is obtained by adding V_m of both layers. It can be noted that in the 1D picture, we do not account for the rotational motion of electrons and hence, direct addition is considered to be a valid approximation. For the AP region, V can be assumed to remain the same as in the CN region. For our calculations, we consider the simplest scenario where an excited X1 binds to one doped electron (trion-like). Developing a full theoretical model for the AP is an open problem in the presence of a lattice and would be an interesting future

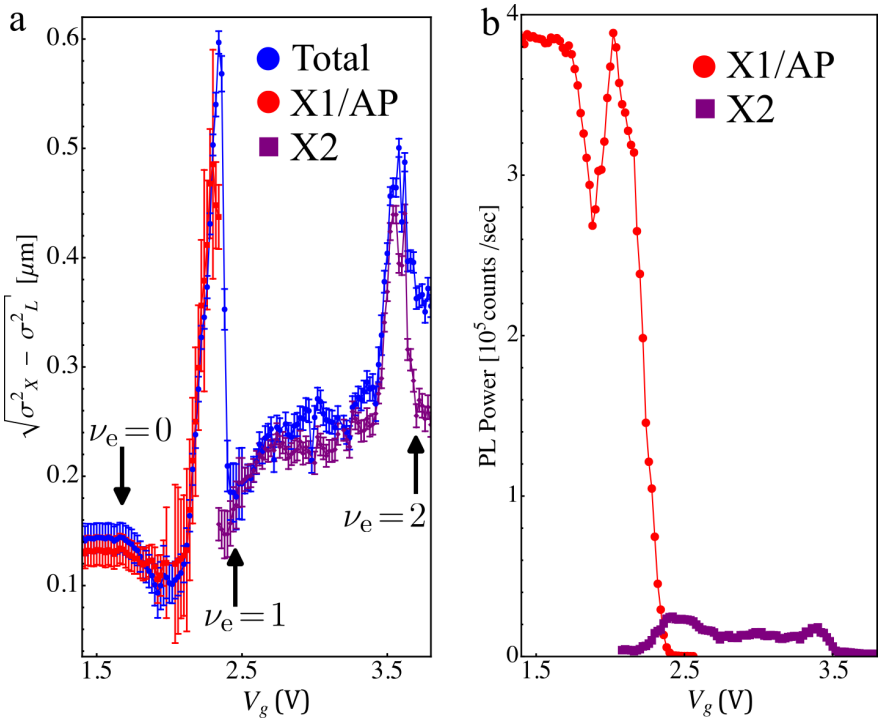

Figure S5: **Spectrally resolved diffusion.** a) Blue, red, and purple markers indicate the net diffusion (no spectral resolution), X1/AP diffusion, and X2 diffusion, respectively. Filling factors are marked with arrows. b) Integrated PL variation of X1/AP and X2 over the doping range indicates similar X1 and X2 intensity near the Mott region.

direction. Here, we assume a trion picture where we can approximate its mass as $2m_e + m_h$. This increase in m leads to a much stronger localization effect in the presence of the moiré lattice. This effect is captured by the increase in m^* indicating slower diffusion of AP than X1.

In the Mott region, electrons in WS_2 crystallize due to strong electron-electron repulsion. However, holes in WSe_2 experience a weak effective potential because of the addition of an out-of-phase periodic potential ($V_{Coul} \sim 88$ meV) exerted by the doped electron lattice (WS_2) on the holes. The obtained V_{Coul} is out-of-phase compared to V_m of the hole layer because the electrons and holes reside in different moiré registries, which are laterally displaced. This leads to a strong suppression in V (~ 12 meV), allowing for non-monogamous hole diffusion.

For X2 diffusion, V for the electron and hole is calculated separately and then added. The potential V for the hole layer remains roughly the same as in the Mott region, as the hole still experiences the strong V_{Coul} due to the electron lattice. However, for the electron layer, there are

Fermionic Region (Diffusing particle)	m (m_0)	V (meV)	m^* (m_0)
CN Region (X1)	0.9	200	182
Low doping (AP)	1.4	200	2800
Mott (hole)	0.4	12	0.4
High Doping (X2)	0.9	66	4.6

Table S1: Effective mass variation with doping

strong repulsive on-site interactions between the doped electron and the excited electron. This effectively increases the energy of the excited electron, which then sees a shallower potential. We approximate V as V_{m} - $U_{\mathrm{e-e}}$, where $U_{\mathrm{e-e}}$ represents the on-site electron-electron repulsions. For H-stacking, this can be approximated as the exciton-electron repulsion, which is observed from PL to be around 46 meV. Therefore, V of 54 meV for the electron layer and 12 meV for the hole layer give an overall V of 66 meV experienced by X2. This leads to an increase in the effective mass (m^*) compared to the Mott region, but it remains orders of magnitude smaller than in the CN region.

Supplementary Note 6. Temperature dependence of Mott gap

We perform temperature-dependent PL measurements to verify the presence of the Mott gap in the entire range of temperatures used for measurements. Figure S6 demonstrates the Mott gap even at 260 K, although the gap reduction is observed with temperature.

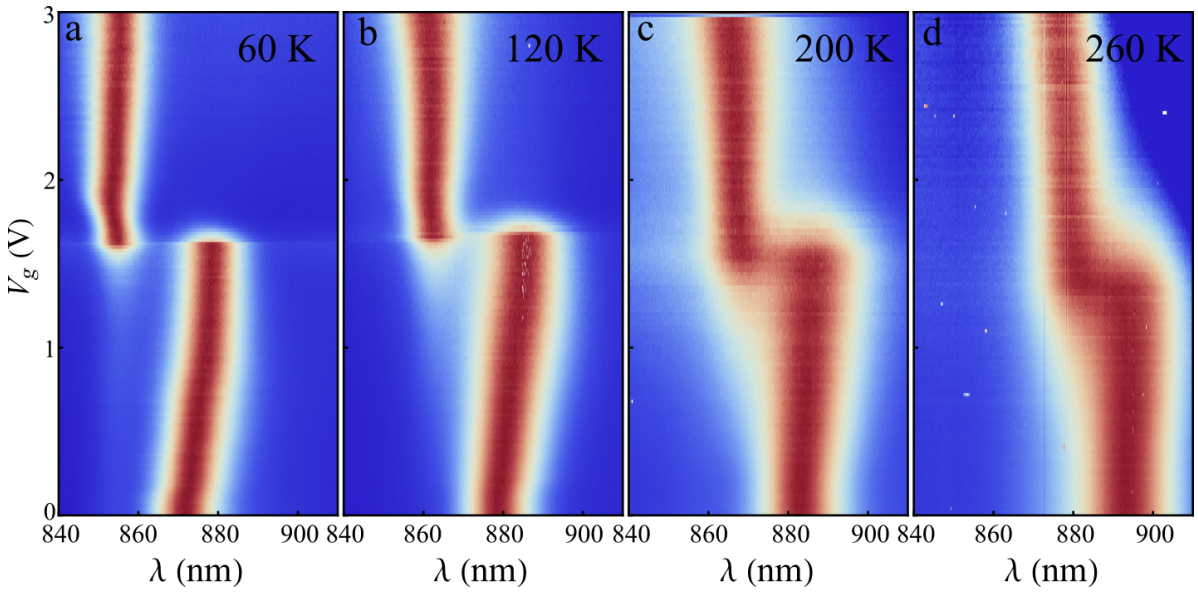

Figure S6: **Temperature dependence of Mott transition.** PL spectra at high temperatures, a) 60 K, b) 120 K, c) 200 K and d) 260 K demonstrate Mott gap. The gap, however, reduces with temperature as expected. Measurements are done at relatively higher pump intensity (300 nW/μm^2).